

Article

Evaluation of High Resolution WRF Solar

Jayesh Thaker ^{1,*}  and Robert Höller ² ¹ Department of Physics, Carl von Ossietzky Universität Oldenburg, 26129 Oldenburg, Germany² School of Engineering, University of Applied Sciences Upper Austria, Stelzhamerstrasse 23, 4600 Wels, Austria

* Correspondence: jayesh.thaker@uni-oldenburg.de; Tel.: +49-15168-797550

Abstract: The amount of solar irradiation that reaches Earth's surface is a key quantity of solar energy research and is difficult to predict, because it is directly affected by the changing constituents of the atmosphere. The numerical weather prediction (NWP) model performs computational simulations of the evolution of the entire atmosphere to forecast the future state of the atmosphere based on the current state. The Weather Research and Forecasting (WRF) model is a mesoscale NWP. WRF solar is an augmented feature of WRF, which has been improved and configured specifically for solar energy applications. The aim of this paper is to evaluate the performance of the high resolution WRF solar model and compare the results with the low resolution WRF solar and Global Forecasting System (GFS) models. We investigate the performance of WRF solar for a high-resolution spatial domain of resolution 1×1 km and compare the results with a 3×3 km domain and GFS. The results show error metrics rMAE {23.14%, 24.51%, 27.75%} and rRMSE {35.69%, 36.04%, 37.32%} for high resolution WRF solar, coarse domain WRF solar and GFS, respectively. This confirms that high resolution WRF solar performs better than coarse domain and in general. WRF solar demonstrates statistically significant improvement over GFS.

Keywords: solar radiation; NWP; GFS; WRF; GHI; solar forecasting

**Citation:** Thaker, J.; Höller, R.

Evaluation of High Resolution WRF

Solar. *Energies* **2023**, *16*, 3518.<https://doi.org/10.3390/en16083518>

Academic Editors: Jesús Polo and

Gabriel López Rodríguez

Received: 5 March 2023

Revised: 3 April 2023

Accepted: 12 April 2023

Published: 18 April 2023



Copyright: © 2023 by the authors. Licensee MDPI, Basel, Switzerland. This article is an open access article distributed under the terms and conditions of the Creative Commons Attribution (CC BY) license (<https://creativecommons.org/licenses/by/4.0/>).

1. Introduction

Installed solar energy capacity has increased rapidly in recent years across the globe. Due to unpredictable weather conditions, the nature of the solar irradiance reaching the ground surface is highly fluctuating and stochastic. As a consequence, forecast challenges emerge and amplify, which requires mitigation to maintain balance between supply and demand on the electrical grid, energy utilities and independent system operators.

The forecast models used for solar irradiance forecasting are diverse and interdisciplinary depending on the prediction horizon, the purpose of the predictions and further applications. Solar forecasting combines many fields such as atmospheric physics, image processing, remote sensing, machine learning and statistics. The development of forecast models often depends on the prediction horizon, the goal of the predictions and the applications. These are broadly classified into three categories depending on the forecast horizon: day-ahead forecasts, intra-day forecasts and intra-hour forecasts. They could also be subdivided into different groups depending on their characteristics and applications. For instance, some methods take into account spatial-temporal features. There are approaches that consider only the intrinsic data features, and some models consider exogenous inputs along with intrinsic features. Models can be either deterministic or probabilistic, depending on the forecast type and applications. Hybrid models apply multiple approaches at once, whereas an ensemble method implements the results of various models. NWP, All-sky imagers (ASI), satellite imaging, statistical analysis, machine learning (ML) and deep learning artificial neural networks (ANN) are among the various methods being investigated in the broad field to accomplish this goal. A brief overview of different approaches and applications of various models is presented in [1].

Most of the NWP models apply radiative transfer models to simulate the transfer of solar radiation through the atmosphere. NWP models use observed meteorological variables, a regional geographic configuration and simulations of the dynamics and physical relationships between the variables in their calculations. In addition, they also account for complex atmospheric chemistry and different physical schemes in time and space steps across the calculation domain. The benefit of using meteorological models is their flexibility of use, which allows them to replicate both the present and the future climatic conditions. They also have a wide range of spatial and temporal coverage. The inclusion of the diurnal cycle, necessary for an accurate depiction of the surface fluxes in a column of atmosphere, was initially the primary goal of the solar parameterizations in the atmospheric models. However, in the current atmospheric forecast models and methods for radiative transfer are solved in each successive layer as well as their interactions with air particles in cumulus and microphysics schemes.

NWP models have been used operationally for weather forecast such as precipitation, storms and cyclones for several decades. Lately, NWP models are extensively applied for solar irradiance forecasts beyond several hours and are critical for day-ahead forecasts and beyond. Day-ahead photovoltaic (PV) power forecasts are an extremely important application for individual variable renewable energy power plants and also for regional load dispatchers to the grid and power distribution companies. This application has gained tremendous importance in scheduling power for bidding in the power market, trading in ancillary service markets, ramp forecasting and grid congestion forecasts. NWP applications for day-ahead solar irradiance and solar power forecasts first gained attention in last two decades [2–6]. Recent studies have demonstrated that the day-ahead forecasts of solar power are advantageous for PV plant owners [7–9], for the optimization of market-bidding in micro-grids [10] and for the operation of electrical networks [11–13].

WRF solar, which is based on a mesoscale WRF, was first introduced in 2015 specifically to predict solar irradiance [14]. WRF is an open-source tool maintained by the National Center for Atmospheric Research (NCAR). WRF has two core variants: the Advanced Research (ARW) [15,16] and the Nonhydrostatic Mesoscale Model (NMM) [17,18]. Our study is exclusively implemented on WRF-ARW core.

The foundation of the WRF-ARW is a Eulerian solver for the fully compressible nonhydrostatic equations. It employs a mass vertical coordinate that varies with height and a third order Runge–Kutta time-integration approach. In order to increase spatial resolution, WRF-ARW offers horizontal nesting of domains (one- or two-way) [19].

The comprehensive physics schemes offered by WRF range from the most basic and effective to the most complex and computationally expensive (microphysics, cumulus convection, atmospheric and surface radiation, planetary boundary layer and land-surface) [19].

WRF solar is an augmented version of WRF specifically designed to improve solar irradiance forecasts. WRF solar is the first mesoscale NWP model specifically developed and intended to respond to the growing demand for forecast variables categorically designed for solar energy applications. The radiative schemes inside the NWP systems calculate the direct normal irradiance (DNI), diffuse (DIF) and GHI components of solar irradiance [14]. WRF solar generates a high frequency time series of all components of solar irradiance. This feature is particularly important to model PV power output ramps due to abrupt change in the surface radiation. It can be programmed for specific applications based on the research and requirement. The latest version of WRF 4.2.2 offers several of the improvements such as:

- (a) Developments to diagnose and extract important atmospheric parameters required by the solar industry;
- (b) Improved representation of aerosol–radiation feedback, with an aerosol-aware MP scheme [20] and an improved cloud–radiation–aerosol parameterization [21,22], Goddard Chemistry Aerosol Radiation and Transport (GOCART) model [23];
- (c) Incorporation of cloud–aerosol interactions;
- (d) Improved cloud-radiation feedback;

(e) A fast radiative transfer model, FARM [24].

Small-scale dynamics and cloud microphysics (evaporation, condensation, etc.) have a significant impact on solar radiation. This can induce a rapid decline in the temporal autocorrelation of solar radiation time series which leads to errors in forecasting [14].

The effects of atmospheric aerosols are not considered in NWP, and standard WRF as the radiative impact of aerosols on GHI is relatively minimal. However, the highly polluted conditions can lead to biases and adversely affect DNI for applications such as concentrated solar power (CSP). WRF solar enables the user to impose changing aerosol optical characteristics in the simulation and takes humidity effects into consideration to account for the aerosol direct influence [14].

WRF solar offers improvement in model performance with special emphasis on surface solar irradiance under clear sky conditions in the following parameters which are not available in WRF: Output DNI and DIF, high frequency output, solar position algorithm including equation of time (EOT) and time varying aerosols for aerosol–radiation feedback, cloud–aerosol feedback and cloud–radiation feedback [14]. WRF solar aims to improve these and other characteristics of the NWP model that is desirable to provide a better shortwave radiation forecasting framework that may enhance the deployment of solar energy facilities.

There has been an increase in interest in the literature recently for using WRF and WRF solar for forecasting solar irradiance in many European and North American locations, reporting relative root mean square error (rRMSE) of about 40% for day-ahead forecasts [3,4,25–27]. However, most of the studies have been undertaken for spatial resolution of 3 km or higher.

This article provides the information about ground measurement data in Section 2.1, a description of the WRF domain and the model setup in Section 2.2, the performance metrics used for the evaluation and comparison of model in Section 3 and an analysis of the results in Section 4.

2. Methodology

2.1. Pyranometer Data

The global horizontal irradiance (GHI) measured data in this analysis is taken from the Kipp and Zonen pyranometer (CMP11) installed at the University of Applied Sciences Upper Austria (FHOOE). The building is located in Wels, Austria (latitude 48.17° N, longitude 14.03° E, elevation 317 m). The granularity of measured GHI is 10 min, which is averaged to hourly data. Model configurations were evaluated for a six-month period starting from 1 January 2021 to 30 June 2021.

Zenith angle correction is applied by filtering GHI data sub-hour for $\theta_z > 80^\circ$ angle of incidence with respect to 1000 W/m² irradiance at normal incidence (0°) as per the technical specification of the pyranometer [1].

The clear sky index is calculated as the ratio of global irradiance $I(t)$ to clear sky global irradiance $I_{cs}(t)$. The Ineichen and Perez clear sky model in PVLIB is used to calculate the clear sky index. The clear sky index is used with a maximum value of 2.0 to account for over-irradiance occurrences that are commonly observed in sub-hourly data due to cloud enhancement and refraction phenomena [28].

$$K_t = \frac{I(t)}{I_{cs}(t)} \quad (1)$$

The hourly clear sky index was divided into six clusters as per Table 1 [1]. HT6 sub-hour refers to early morning sun rise and late evening sunset hours when the clear sky index is greater than 1.

Likewise, the five types of day type classification (DT1, DT2, DT3, DT4, DT5) were generated by first truncating the maximum value K_t to 1 for HT6 and calculating the daily average value K_t by using the same criteria as per Table 1 [1].

Table 1. Hour type classification based on CSI.

Class	Type	CSI Range
HT1	Overcast	$0 \leq K_t < 0.3$
HT2	Highly cloudy	$0.3 \leq K_t < 0.5$
HT3	Cloudy	$0.5 \leq K_t < 0.7$
HT4	Mostly Clear	$0.7 \leq K_t < 0.9$
HT5	Clear	$0.9 \leq K_t \leq 1.0$
HT6	Sub-hour	$K_t > 1.0$

2.2. WRF Model Configuration

This paper compares and evaluates the performance of nested high spatial resolution and a single coarse domain setup. The domain decomposition is illustrated in Figure 1.

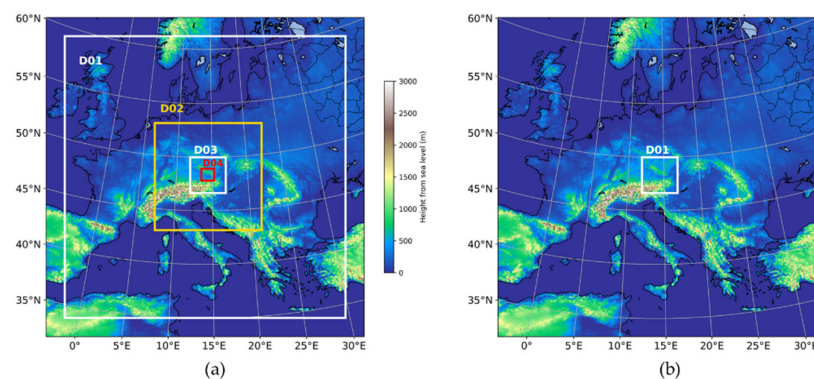


Figure 1. WRF domain setup (a) high resolution four nested domains (4D); (b) coarse single domain (1D).

Four domains are constructed as part of the nested domain 4D, each with a horizontal spatial resolution of 27, 9, 3 and 1 km, one-way feedback. The outer domain D01 is composed of 106×106 cells, whereas the domains D02 and D03 are composed of 121×121 cells, and the innermost domain D04 is composed of 130×121 cells. Single domain D1 is designed with a horizontal spatial resolution of 3 km with 130×121 cells. The ground measurement site for both domains is approximately at the center.

The updated Kain–Fritsch cumulus method is applied in the two outer domains D01 and D02 of D4 because convective clouds are anticipated to be explicitly resolved in the two smaller inside domains D03 and D04 [25,29]. The unified Noah land-surface model [29,30], the second Mellor–Yamada–Nakanishi–Niino (MYNN2) planetary boundary layer scheme [31] and the RRTMG longwave scheme [32] are all used in both configurations. The aerosol aware Thomson microphysics and the aerosol aware RRTMG shortwave scheme implemented in WRF solar are then applied [21]. The aerosols are classified into two species: hygroscopic and non-hygroscopic aerosols. The Goddard Chemistry Aerosol Radiation and Transport (GOCART) model provides three-dimensional monthly climatological data from which the aerosol concentrations are initialized for both configurations [33]. Both domain experiments use vertical 34 metgrid levels and 4 soil levels. For 4D, the evaluation of the WRF forecast is carried out for the innermost domain (D04) which has a time step of 1 s, whereas for single domain 1D the time step is 5 s. GFS data from NCEP archive at temporal resolution of 3 h and spatial resolution of 0.250×0.250 (NCEP GFS ds084.1) are used to initialize both WRF models for the input and boundary conditions [34]. WRF models are initialized with 0 UTC input data to meet and stabilize the initial boundary conditions. The objective is to produce forecasts up to 21 h UTC for each hour for the following day.

The detailed experimental setup of the WRF preprocessing system, WPS and WRF run for high resolution nested domains are provided in the respective namelist files in Appendices A and B for viewers.

2.3. Performance Metrics

The three most widely used metrics for point forecast accuracy are the mean bias error (MBE), the mean absolute error (MAE) and the root mean square error (RMSE). In this paper, the focus is on MAE and RMSE considering that these metrics reflect the financial impact of forecast errors most appropriately for most grid operators, energy utilities and individual operators [1]. The performance of these two configurations of domain setup and GFS is compared by mean absolute error (MAE) and the root mean square error (RMSE).

$$MAE = \frac{1}{N} \sum_{i=1}^N |y_i - \hat{y}_i| \quad (2)$$

$$RMSE = \frac{1}{N} \sqrt{\sum_{i=1}^N (y_i - \hat{y}_i)^2} \quad (3)$$

where N is the number of forecasts, and y is the true value, and \hat{y} is the forecast value.

The relative MAE (rMAE) and RMSE (rRMSE) are calculated by dividing the respective metrics by the average value of the measured GHI (y) for the test period under consideration.

3. Results and Discussion

This section presents an overview and comparison of GHI forecast from GFS and the two variants of WRF solar with ground measurement data. In this paper, hourly GHI forecasts from two configurations of WRF solar model and GFS were evaluated and compared in terms of rMAE and rRMSE against ground measurement GHI data collected at Wels, Austria.

Figure 2 shows the violin plots along with swarm plots of data points therein for ground measurement versus GFS, high resolution WRF solar 4-domains and single domain forecast data for different categories of hour types. It is clearly evident that GFS forecast data are highly positively biased for HT1, HT2, HT3 and HT4, which also results in a positive bias for WRF solar prediction, as WRF solar uses GFS as input data for initialization of the models. It may also be noted that GFS is slightly negatively biased for HT6 compared to ground measurement data. The maximum GHI value predicted by GFS for HT6 during the test period is 923.2 W/m², and coarse domain WRF solar is 954.6 W/m² versus a ground measurement value of 984.5. This demonstrates that WRF solar is capable of capturing the enhanced value of GHI under sub-hour clear sky day conditions.

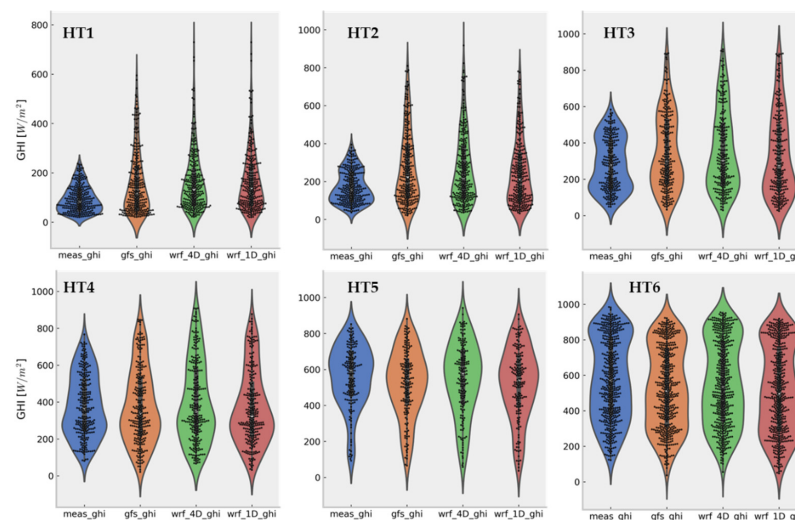


Figure 2. Violin swarm plots of ground measurement data with GFS, WRF solar 4 domains and 1 domain.

The variation of relative rMAE and rRMSE shown in Figure 3 illustrates that WRF solar corrects the forecast bias of GFS substantially for all different hour types. It is noteworthy that high resolution WRF solar domain 4 outperforms single domain WRF solar for HT1, HT5 and HT6 where there is minimum variability. However, under the high variability of cloud movements in HT2, HT3 and HT4, single domain low resolution WRF solar resolves cloud movement more effectively and performs better compared with high resolution 4 domain WRF solar.

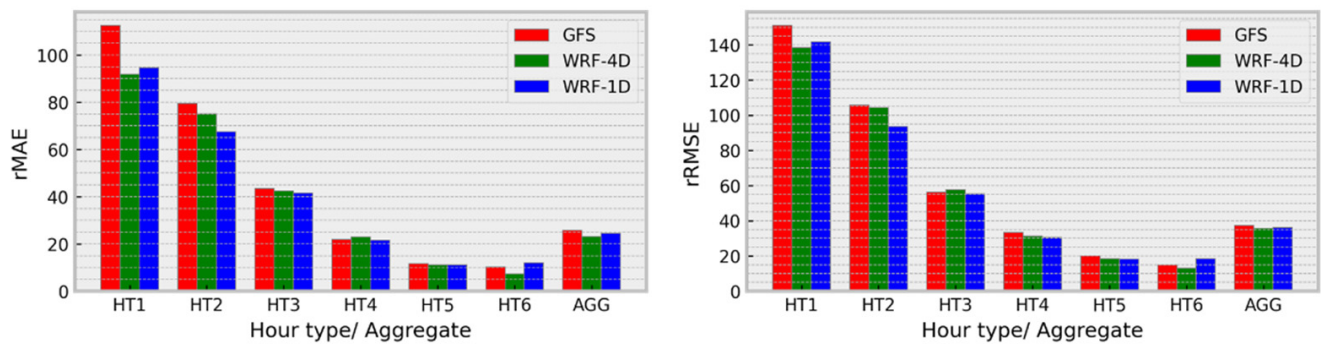


Figure 3. Variation of rMAE and rRMSE for different hour types and overall aggregate for the duration.

Overall, the aggregate performance of high resolution WRF solar nested 4 domains is statistically better compared to single domain while both WRF solar results are significantly better compared to GFS as shown in AGG. High resolution WRF solar nested domain yields rMAE (23.14%) and rRMSE (35.69%) compared to the coarse domain (24.51%), (36.04%) and GFS (25.75%), (37.32%), respectively.

Figure 4 shows the variation of error metrics for the three models for different forecast day types based on GFS forecast value of K_t . It is clearly evident that high resolution WRF solar outperforms all of the day-type categories and in particular for the overcast days where the improvement is significantly higher.

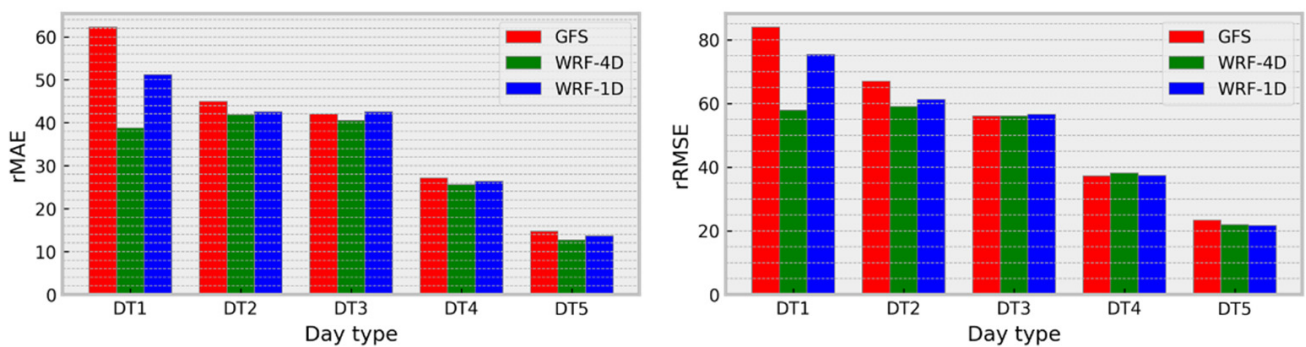


Figure 4. Variation of rMAE and rRMSE for different day types.

Figure 5a shows the intra-data hourly variation of ground measurement GHI along with forecast GHI from GFS, high resolution WRF solar four nested domains and a single domain with an event marked as red circle; (b) shows GHI mapping for the corresponding event from the inner most high resolution WRF solar; (c) shows the same for the single domain; and (d) shows the satellite image of cloud obtained from NASA’s Moderate Resolution Imaging Spectroradiometer, MODIS, satellite with the point of interest in the center marked by red cross. MODIS provides satellite images twice a day, and the image at 12 noon is used for comparison of GHI with clouds for the event. The satellite images from MODIS are chosen for GHI comparison as its spatial resolution is 1 km. The image area shown in the figure are (a) 130×121 km, (b) 390×363 km and

(c) 120×120 km, and the red square in satellite image (c) is 20×20 km with center at ground measurement center in Wels.

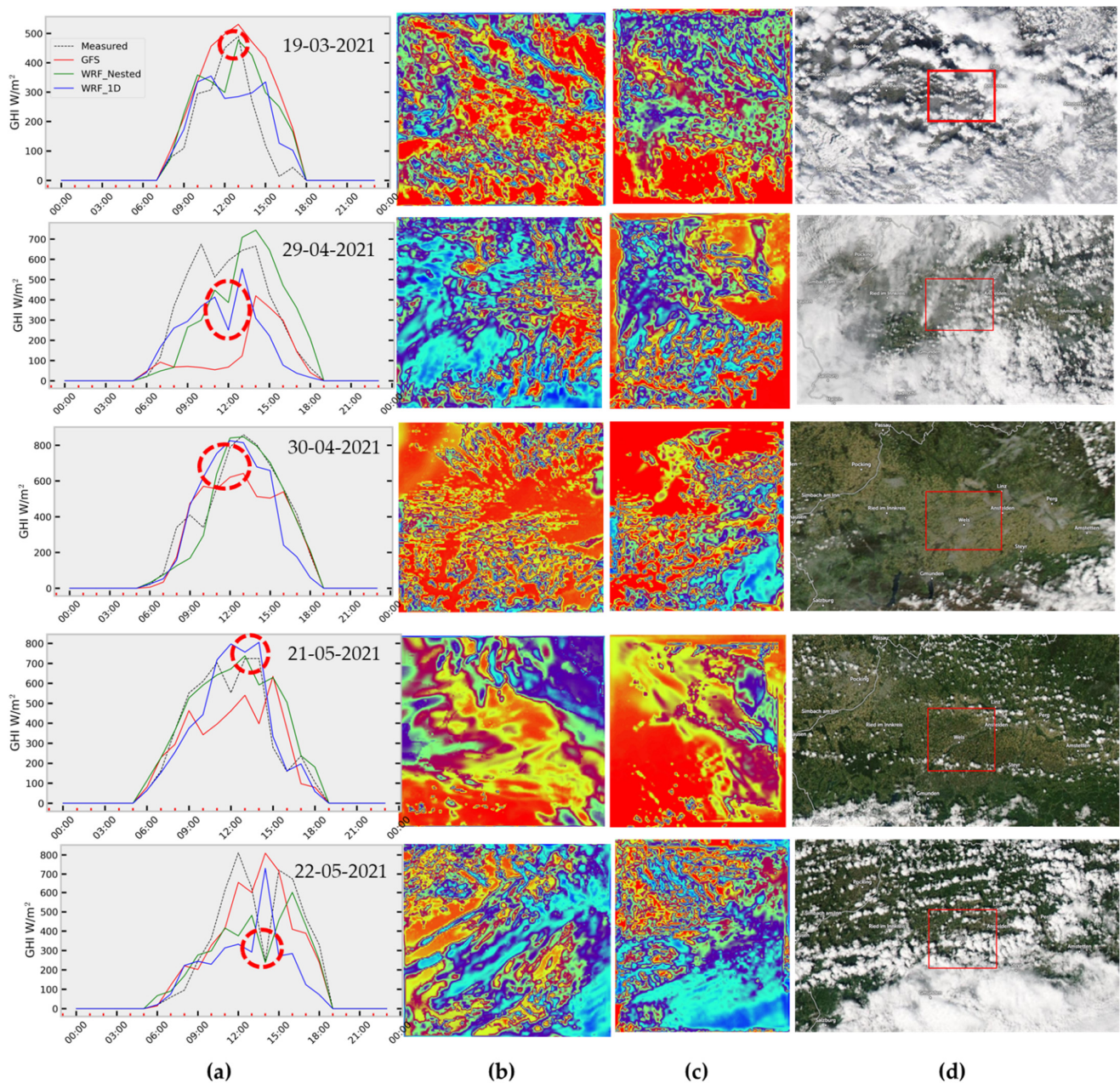


Figure 5. (a) Intra-day hourly variation of GHI with an event marked by red circle, (b) GHI mapping of high resolution 4-domains for an event, (c) GHI mapping of single domain for an event, (d) high spatial resolution (4 km) MODIS satellite image at 12 noon.

It is evident that high resolution WRF captures clear sky days (30 April 2021) most effectively and also the overcast event as shown on 22 May 2021 very well. Furthermore, nested high resolution WRF resolves clouds for clear sky better compared with single domain as illustrated on 29 April 2021. However, 4D fails to resolve rapid cloud movements during cloudy and partly cloudy days compared with 1D as illustrated on 19 March 2021 between 15:00 to 18:00 h and on 21 May 2021 between 12:00 to 15:00 h, resulting in 1D performing better under high cloudy variation. In general, it was also observed that 4D is more positively biased compared with 1D.

4. Conclusions and Outlook

NWPs are specially designed for day-ahead weather and solar irradiance forecasts. However, even the most advanced NWP models remain relatively inaccurate despite recent improvements due to uncertain initial boundary conditions.

In this paper, hourly GHI forecasts from two configurations of WRF solar model and GFS were assessed and compared in terms of rMAE and rRMSE against ground measurement GHI data collected at Wels, Austria. This paper has demonstrated the potential of using nested high resolution WRF solar to significantly improve the forecast accuracy of NWP models. The forecasting accuracy can be further improved by an ensemble of nested high resolution WRF solar with coarse single domain WRF solar based on the cloud variability under clear sky or overcast conditions and under cloudy conditions. Further, WRF solar high resolution needs to be investigated using the model data from European Centre for Medium-Range Weather Forecasts (ECMWF) to initialize the model instead of GFS.

Although WRF solar is able to improve the forecast accuracy of GFS, both global and mesoscale models remain highly correlated and systematically fail to forecast completely overcast conditions. This is primarily due to propagation of numerical errors and approximations caused by unknown initial boundary conditions and highly unpredictable atmospheric phenomenon coupled with complex local orography. Further post-processing methods known as model output statistics (MOS) can be applied to reduce the bias and minimize these errors which typically exhibit systematic and frequent pattern.

It is noteworthy that the computational cost of nested high resolution WRF solar on a standard duo-core i5 processor desktop is very high, and it effectively takes an hour to process a forecast for one hour. It is therefore strongly recommended to use WRF solar either on cloud or multi-parallel processors.

Author Contributions: Conceptualization, J.T. and R.H.; Formal Analysis, J.T.; Software, J.T.; Visualization, J.T.; Validation, J.T.; Writing—Original Draft Preparation, J.T.; Writing—Review and Editing, R.H.; Project Administration, R.H.; Supervision, R.H. All authors have read and agreed to the published version of the manuscript.

Funding: This research received no external funding.

Institutional Review Board Statement: Not applicable.

Informed Consent Statement: Not applicable.

Data Availability Statement: Not applicable.

Acknowledgments: We thank Manajit Sengupta for his valuable advice, Xiaodong Chen for his assistance in generating WRF domain plots Figure 1 and Douglas Vaught for reviewing the manuscript.

Conflicts of Interest: The authors declare no conflict of interest.

Appendix A. WPS Namelist File

```
&share
  wrf_core = 'ARW',
  max_dom = 4,
  start_date = '2021-04-08_00:00:00', '2021-04-08_00:00:00', '2021-04-08_00:00:00',
'2021-04-08_00:00:00',
  end_date = '2021-04-08_21:00:00', '2021-04-08_21:00:00', '2021-04-08_21:00:00', '2021-
04-08_21:00:00',
  interval_seconds = 10800,
  io_form_geogrid = 2,
  /

&geogrid
  parent_id           = 0, 1, 2, 3,
```

```

parent_grid_ratio = 1, 3, 3, 3,
i_parent_start   = 1, 34, 40, 38,
j_parent_start   = 1, 33, 42, 42,
e_we             = 106, 121, 121, 130,
e_sn            = 106, 121, 121, 121
!
!!!!!!!!!!!!!!!!!!!!!!!!!!!! IMPORTANT NOTE !!!!!!!!!!!!!!!!!!!!!!!!!!!!!
! The default datasets used to produce the MAXSNOALB and ALBEDO12M
! fields have changed in WPS v4.0. These fields are now interpolated
! from MODIS-based datasets.
!
! To match the output given by the default namelist.wps in WPS v3.9.1,
! the following setting for geog_data_res may be used:
!
! geog_data_res = 'maxsnowalb_ncep+albedo_ncep+default', '
! maxsnowalb_ncep+albedo_ncep+default',
!
!!!!!!!!!!!!!!!!!!!!!!!!!!!! IMPORTANT NOTE !!!!!!!!!!!!!!!!!!!!!!!!!!!!!
!
geog_data_res = 'default', 'default',

dx = 27000,
dy = 27000,
map_proj = 'lambert',
ref_lat = 48.161665
ref_lon = 14.027737,
truelat1 = 60,
truelat2 = 35,
stand_lon = 14.027737,
geog_data_path = '/home/jayesh/Build_WRF/WPS_GEOG'
/

&ungrib
  out_format = 'WPS',
  prefix = 'GFS',
/

&metgrid
  fg_name = 'GFS'
  io_form_metgrid = 2,
  constants_name = 'QNWFA_QNIFA_SIGMA_MONTHLY.dat'
//2021-03-30_00:00:00', '2021-03-30_00:00:00', '2021-03-30_00:00:00',

```

Appendix B. WRF Run Namelist File

```

&time_control
run_days           = 0,
run_hours          = 21,
run_minutes        = 0,
run_seconds        = 0,
start_year         = 2021,2021,2021,2021,
start_month        = 04,04,04,04,
start_day          = 08,08,08,08,
start_hour         = 00,00,00,00,
end_year           = 2021,2021,2021,2021,

```

```

end_month           = 04,04,04,04,
end_day             = 08,08,08,08,
end_hour            = 21,21,21,21,
interval_seconds    = 10,800,

input_from_file     = .true.,.true.,.true.,.true.,
history_interval    = 180,60,30,30,
frames_per_outfile  = 1000,1000,1000,1000,
restart              = .false.,
restart_interval     = 1440,
io_form_history      = 2
io_form_restart      = 2
io_form_input        = 2
io_form_boundary     = 2
io_form_auxinput1    = 2
io_form_auxhist2     = 2
debug_level         = 0
/

&domains
time_step           = 81,
time_step_fract_num = 0,
time_step_fract_den = 1,
max_dom             = 4,
s_we                = 1,
e_we                = 106, 121, 121, 130,
e_sn                = 106, 121, 121, 121,
s_vert              = 1, 1, 1, 1,
e_vert              = 45, 45, 45,45,
eta_levels = 1.00000, 0.99629, 0.99257, 0.98879,
0.98486, 0.98071, 0.97622, 0.97130,
0.96585, 0.95977, 0.95299, 0.94540,
0.93692, 0.92744, 0.91686, 0.90507,
0.89195, 0.87737, 0.86120, 0.84331,
0.82356, 0.80181, 0.77793, 0.75181,
0.72335, 0.69246, 0.65911, 0.62329,
0.58506, 0.54455, 0.50195, 0.45755,
0.41175, 0.36503, 0.31802, 0.27144,
0.22617, 0.18317, 0.14344, 0.10788,
0.07710, 0.05132, 0.03028, 0.01343,
0.00000,
p_top_requested     = 5000,
num_metgrid_levels  = 34,
num_metgrid_soil_levels = 4,
dx                  = 27,000,
dy                  = 27,000,
grid_id             = 1, 2, 3, 4,
parent_id           = 0, 1, 2, 3,
i_parent_start      = 1, 34, 40, 38,
j_parent_start      = 1, 33, 42, 42,
parent_grid_ratio    = 1, 3, 3, 3,
parent_time_step_ratio = 1, 3, 3, 3,
feedback            = 1,
smooth_option       = 0,
max_ts_locs         = 1,

```

```

wif_input_opt = 1
num_wif_levels = 30
/

&physics
mp_physics      = 28, 28, 28, 28,
ra_lw_physics  = 4,  4,  4,  4,
ra_sw_physics  = 4,  4,  4,  4,
radt           = 27,  9,  3,  1,
sf_sfclay_physics = 1,  1,  1,  1,
sf_surface_physics = 2,  2,  2,  2,
bl_pbl_physics = 5,  5,  5,  5,
bldt           = 0,  0,  0,  0,
bl_mynn_tkeadvect = .true.,.true.,.true.,.true.,
cu_physics     = 1,  1,  0,  0,
cu_rad_feedback = .true., true., false.,false.,
cudt           = 5,  5,  0,  0,
bl_mynn_edmf   = 0,  0,  0,  0,
shcu_physics   = 5,  5,  5,  5,
isfflx = 1,
ifsnow = 1,
icloud = 1,
icloud_bl = 1,
kfeta_trigger = 1,
bl_mynn_cloudmix = 1,  1,  1,  1,
bl_mynn_cloudpdf = 1,
num_land_cat    = 21,
num_soil_layers = 4,
sf_urban_physics = 0,  0,  0,  0,
num_land_cat    = 21,
aer_opt = 3,
swint_opt = 2,
use_aero_icbc = .true.,
usemonalb = .true.,
/

&fdda
/

&dynamics
hybrid_opt      = 2,
w_damping       = 1,
diff_opt        = 1,  1,  1,  1,
km_opt          = 4,  4,  4,  4,
diff_6th_opt    = 0,  0,  0,  0,
diff_6th_factor = 0.12, 0.12, 0.12, 0.12,
base_temp       = 290.
damp_opt        = 3,
zdamp           = 5000., 5000., 5000., 5000.,
dampcoef        = 0.2, 0.2, 0.2,  0.2,
khdif           = 0,  0,  0,  0,
kvdif           = 0,  0,  0,  0,
non_hydrostatic = .true., .true., .true., .true.,
moist_adv_opt   = 1,  1,  1,  1,

```

```

scalar_adv_opt          = 1,    1,    1,    1,
gwd_opt                 = 1,    1,    1,    1,
/

&bdy_control
spec_bdy_width          = 5,
spec_zone                = 1,
relax_zone               = 4,
specified                = .true.,.true.,true.,true.,
nested                   = .false.,.false.,.false.,.false.,
/

&grib2
/

&namelist_quilt
nio_tasks_per_group = 0,
nio_groups = 1,
/
&diags
solar_diagnostics = 1,
/

```

References

1. Thaker, J.; Höller, R. Hybrid Numerical Ensemble Method and Comparative Study for Solar Irradiance Forecasting. In Proceedings of the 8th World Conference on Photovoltaic Energy Conversion, Milan, Italy, 26–30 September 2022; pp. 1276–1284. [\[CrossRef\]](#)
2. Zamora, R.J.; Dutton, E.G.; Trainer, M.; McKeen, S.A.; Wilczak, J.M.; Hou, Y.-T. The Accuracy of Solar Irradiance Calculations Used in Mesoscale Numerical Weather Prediction. *Mon. Weather Rev.* **2005**, *133*, 783–792. [\[CrossRef\]](#)
3. Lorenz, E.; Remund, J.; Müller, S.C.; Traunmüller, W.; Steinmaurer, G.; Pozo, D.; Ruiz-Arias, J.A.; Lara Fanego, V.; Ramirez, L.; Romeo, M.G.; et al. Benchmarking of Different Approaches to Forecast Solar Irradiance. In Proceedings of the 24th European Photovoltaic Solar Energy Conference, Hamburg, Germany, 21–25 September 2009; pp. 4199–4208. [\[CrossRef\]](#)
4. Lara-Fanego, V.; Ruiz-Arias, J.; Pozo-Vázquez, D.; Santos-Alamillos, F.; Tovar-Pescador, J. Evaluation of the WRF model solar irradiance forecasts in Andalusia (southern Spain). *Sol. Energy* **2012**, *86*, 2200–2217. [\[CrossRef\]](#)
5. Mathiesen, P.; Kleissl, J. Evaluation of numerical weather prediction for intra-day solar forecasting in the continental United States. *Sol. Energy* **2011**, *85*, 967–977. [\[CrossRef\]](#)
6. Perez, R.; Lorenz, E.; Pelland, S.; Beauharnois, M.; Van Knowe, G.; Hemker, K., Jr.; Heinemann, D.; Remund, J.; Müller, S.C.; Traunmüller, W.; et al. Comparison of numerical weather prediction solar irradiance forecasts in the US, Canada and Europe. *Sol. Energy* **2013**, *94*, 305–326. [\[CrossRef\]](#)
7. Kaur, A.; Nonnenmacher, L.; Pedro, H.T.; Coimbra, C.F. Benefits of solar forecasting for energy imbalance markets. *Renew. Energy* **2016**, *86*, 819–830. [\[CrossRef\]](#)
8. Reindl, T.; Walsh, W.; Yanqin, Z.; Bieri, M. Energy meteorology for accurate forecasting of PV power output on different time horizons. *Energy Procedia* **2017**, *130*, 130–138. [\[CrossRef\]](#)
9. Cornaro, C.; Pierro, M.; Bucci, F. Master optimization process based on neural networks ensemble for 24-h solar irradiance forecast. *Sol. Energy* **2015**, *111*, 297–312. [\[CrossRef\]](#)
10. Alessandrini, S.; Davò, F.; Sperati, S.; Benini, M.; Monache, L.D. Comparison of the economic impact of different wind power forecast systems for producers. *Adv. Sci. Res.* **2014**, *11*, 49–53. [\[CrossRef\]](#)
11. Martinez-Anido, C.B.; Botor, B.; Florita, A.R.; Draxl, C.; Lu, S.; Hamann, H.F.; Hodge, B.-M. The value of day-ahead solar power forecasting improvement. *Sol. Energy* **2016**, *129*, 192–203. [\[CrossRef\]](#)
12. Ghosh, S.; Rahman, S.; Pipattanasomporn, M. Distribution Voltage Regulation through Active Power Curtailment with PV Inverters and Solar Generation Forecasts. *IEEE Trans. Sustain. Energy* **2016**, *8*, 13–22. [\[CrossRef\]](#)
13. Gandhi, O.; Zhang, W.; Rodriguez-Gallegos, C.D.; Verbois, H.; Sun, H.; Reindl, T.; Srinivasan, D. Local reactive power dispatch optimisation minimising global objectives. *Appl. Energy* **2020**, *262*, 114529. [\[CrossRef\]](#)
14. Jimenez, P.A.; Hacker, J.P.; Dudhia, J.; Haupt, S.E.; Ruiz-Arias, J.A.; Gueymard, C.A.; Thompson, G.; Eidhammer, T.; Deng, A. WRF-Solar: Description and Clear-Sky Assessment of an Augmented NWP Model for Solar Power Prediction. *Bull. Am. Meteorol. Soc.* **2016**, *97*, 1249–1264. [\[CrossRef\]](#)

15. Skamarock, W.C.; Klemp, J.B.; Dudhia, J.; Gill, D.O.; Barker, D.M.; Duda, M.G.; Huang, X.-Y.; Wang, W.; Powers, J.G. *A Description of the Advanced Research WRF Version 3*; NCAR Technical Note NCAR/TN-475+STR; University Corporation for Atmospheric Research: Boulder, CO, USA, 2008. [[CrossRef](#)]
16. Skamarock, W.C.; Klemp, J.B.; Dudhia, J.; Gill, D.O.; Zhiquan, L.; Berner, J.; Wang, W.; Powers, J.G.; Duda, M.G.; Barker, D.M.; et al. *A Description of the Advanced Research WRF Model Version 4*; No. NCAR/TN-556+STR; University Corporation for Atmospheric Research: Boulder, CO, USA, 2019. [[CrossRef](#)]
17. Janjic, Z.I. A nonhydrostatic model based on a new approach. *Meteorol. Atmos. Phys.* **2003**, *82*, 271–285. [[CrossRef](#)]
18. Janjic, Z.I.; Gerrity, J.P., Jr.; Nickovic, S. An Alternative Approach to Nonhydrostatic Modeling. *Mon. Weather Rev.* **2001**, *129*, 1164–1178. [[CrossRef](#)]
19. Gentile, S.; Di Paola, F.; Cimini, D.; Gallucci, D.; Geraldini, E.; Larosa, S.; Nilo, S.T.; Ricciardelli, E.; Ripepi, E.; Viggiano, M.; et al. 3D-VAR Data Assimilation of SEVIRI Radiances for the Prediction of Solar Irradiance in Italy Using WRF Solar Mesoscale Model—Preliminary Results. *Remote Sens.* **2020**, *12*, 920. [[CrossRef](#)]
20. Thompson, G.; Eidhammer, T. A Study of Aerosol Impacts on Clouds and Precipitation Development in a Large Winter Cyclone. *J. Atmos. Sci.* **2014**, *71*, 3636–3658. [[CrossRef](#)]
21. Jiménez, P.A.; Alessandrini, S.; Haupt, S.E.; Deng, A.; Kosovic, B.; Lee, J.A.; Monache, L.D. The Role of Unresolved Clouds on Short-Range Global Horizontal Irradiance Predictability. *Mon. Weather Rev.* **2016**, *144*, 3099–3107. [[CrossRef](#)]
22. Ruiz-Arias, J.A.; Quesada-Ruiz, S.; Fernández, E.F.; Gueymard, C.A. Optimal combination of gridded and ground-observed solar radiation data for regional solar resource assessment. *Sol. Energy* **2015**, *112*, 411–424. [[CrossRef](#)]
23. Chin, M.; Ginoux, P.; Kinne, S.; Torres, O.; Holben, B.N.; Duncan, B.N.; Martin, R.V.; Logan, J.A.; Higurashi, A.; Nakajima, T. Tropospheric Aerosol Optical Thickness from the GOCART Model and Comparisons with Satellite and Sun Photometer Measurements. *J. Atmos. Sci.* **2002**, *59*, 461–483. [[CrossRef](#)]
24. Xie, Y.; Sengupta, M.; Dudhia, J. A Fast All-sky Radiation Model for Solar applications (FARMS): Algorithm and performance evaluation. *Sol. Energy* **2016**, *135*, 435–445. [[CrossRef](#)]
25. Diagne, M.; David, M.; Boland, J.; Schmutz, N.; Lauret, P. Post-processing of solar irradiance forecasts from WRF model at Reunion Island. *Energy Procedia* **2014**, *57*, 1364–1373. [[CrossRef](#)]
26. Balog, I.; Podrascanin, Z.; Spinelli, F.; Caputo, G.; Siviero, R.; Benedetti, A. Hourly forecast of solar radiation up to 48h with two runs of weather research forecast model over Italy. *AIP Conf. Proc.* **2019**, *2126*, 190004. [[CrossRef](#)]
27. Perez, R.; Ho, T. Solar Anywhere Forecasting. In *Solar Energy Forecasting and Resource Assessment*; Kleissl, J., Ed.; Elsevier: Amsterdam, The Netherlands, 2013.
28. Available online: <https://pvlib-python.readthedocs.io/en/v0.4.3/generated/pvlib.clearsky.ineichen.html> (accessed on 10 December 2022).
29. Kain, J.S. The Kain-Fritsch Convective Parameterization: An Update. *J. Appl. Meteorol.* **2004**, *43*, 170–181. [[CrossRef](#)]
30. Ek, M.B.; Mitchell, K.E.; Lin, Y.; Rogers, E.; Grunmann, P.; Koren, V.; Gayno, G.; Tarpley, J.D. Implementation of Noah land surface model advances in the National Centers for Environmental Prediction operational mesoscale Eta model. *J. Geophys. Res. Atmos.* **2003**, *108*, 8851. [[CrossRef](#)]
31. Nakanishi, M.; Niino, H. An Improved Mellor-Yamada Level-3 Model: Its Numerical Stability and Application to a Regional Prediction of Advection Fog. *Bound.-Layer Meteorol.* **2006**, *119*, 397–407. [[CrossRef](#)]
32. Iacono, M.J.; Delamere, J.S.; Mlawer, E.J.; Shephard, M.W.; Clough, S.A.; Collins, W.D. Radiative forcing by long-lived greenhouse 149 gases: Calculations with the AER radiative transfer models. *J. Geo-Phys. Res. Atmos.* **2008**, *113*, D13103. [[CrossRef](#)]
33. Ginoux, P.; Chin, M.; Tegen, I.; Prospero, J.M.; Holben, B.; Dubovik, O.; Lin, S.-J. Sources and distributions of dust aerosols simulated with the GOCART model. *J. Geophys. Res. Atmos.* **2001**, *106*, 20255–20273. [[CrossRef](#)]
34. Available online: https://www2.mmm.ucar.edu/wrf/users/download/free_data.html (accessed on 15 June 2022).

Disclaimer/Publisher’s Note: The statements, opinions and data contained in all publications are solely those of the individual author(s) and contributor(s) and not of MDPI and/or the editor(s). MDPI and/or the editor(s) disclaim responsibility for any injury to people or property resulting from any ideas, methods, instructions or products referred to in the content.